Available online at www.sciencedirect.com
ScienceDirect
Ceramics International 35 (2009) 2877–2883
CERAMICS INTERNATIONAL
www.elsevier.com/locate/ceramint

Thermal and mechanical properties of $LaNbO_4$-based ceramics

Tommy Mokkelbost [a,1], Hilde Lea Lein [a], Per Erik Vullum [b], Randi Holmestad [b], Tor Grande [a], Mari-Ann Einarsrud [a,*]

[a] Department of Materials Science and Engineering, Norwegian University of Science and Technology, N-7491 Trondheim, Norway
[b] Department of Physics, Norwegian University of Science and Technology, N-7491 Trondheim, Norway

Received 22 January 2009; received in revised form 14 February 2009; accepted 27 March 2009
Available online 24 April 2009

Abstract

Thermal and mechanical properties of polycrystalline $La_{1-x}A_xNbO_4$ ($x = 0$, 0.005, 0.02 and A = Ca, Sr and Ba) are reported. The materials possess a ferroelastic to paraelastic phase transition close to 500 °C, and the linear thermal expansion is significantly lower ($\sim 8.6 \pm 0.5 \times 10^{-6}$ °C^{-1}) for the paraelastic phase compared to the ferroelastic phase ($\sim 15 \pm 3 \times 10^{-6}$ °C^{-1}). The hardness was significantly higher for acceptor doped materials (~6 GPa) compared to pure $LaNbO_4$ (~3 GPa) due to a significantly smaller average grain size. The fracture toughness of $La_{0.98}Sr_{0.02}NbO_4$, measured by single edge V-notched beam method, was 1.7 ± 0.2 MPa m$^{1/2}$ independent of temperature up to 600 °C. The ferroelastic properties of the materials were confirmed by non-linear relationships between stress and strain during compression/decompression, a remnant strain after decompression and the presence of ferroelastic domains. The mechanical properties of $LaNbO_4$-based materials are discussed with focus on ferroelasticity, microcracking due to crystallographic anisotropy and pinning of ferroelastic domain boundaries.

Keywords: C. Mechanical properties; D. Niobates

1. Introduction

$LaNbO_4$-based ceramics have been shown to be promising candidates for intermediate temperature proton conducting electrolytes with potential applications in, e.g. solid oxide fuel cells and hydrogen sensors [1]. $LaNbO_4$ undergoes a monoclinic to tetragonal phase transition at ~500 °C [2–5] and is ferroelastic in the low temperature monoclinic phase [6]. Compared to the state-of-the-art proton conductors, such as Sr- and Ba-cerates and zirconates [7], $LaNbO_4$-based materials are stable in CO_2/H_2O atmosphere, but they exhibit lower proton conduction, $\sim 10^{-3}$ S/cm versus $\sim 10^{-2}$ S/cm [8–10]. To achieve satisfactory current densities in specific applications it is therefore necessary to decrease the electrolyte thickness into the sub-100 μm range giving large constraints on the material properties with respect to stability and robustness. An understanding of the mechanical properties of these materials is therefore essential. So far there are only a few reports concerning the mechanical properties of polycrystalline $LaNbO_4$. A 3-point bending strength of 35 MPa was measured for pure $LaNbO_4$ [11], and the material (prepared by pulse electric current sintering) was observed to fracture along grain boundaries. The relatively large grain size of the material together with a crystallographic anisotropy indicated that low mechanical strength was due to microcracking. Jian and Wayman [12] observed the non-linear stress–strain behavior of polycrystalline $LaNbO_4$ due to ferroelasticity during compression.

The aim of this work was to study thermal and mechanical properties of selected $LaNbO_4$-based materials prepared by spray pyrolysis from powders. The sintering properties of the powders and transport properties of the materials have been reported previously [13]. Thermal expansion, hardness, stress–strain relationship during compression and fracture toughness were studied. Special attention was devoted to the temperature dependence of the stress–strain relationship and fracture toughness. In addition, the domain structure was studied by transmission electron microscopy (TEM) to relate ferroelasticity to the mechanical properties.

* Corresponding author.
E-mail address: mari-ann.einarsrud@material.ntnu.no (M.-A. Einarsrud).
[1] Present address: SINTEF Materials and Chemistry, Trondheim, Norway.

0272-8842/$36.00
doi:10.1016/j.ceramint.2009.03.041

2. Experimental

2.1. Materials preparation

Sub-micron powders (0.1 μm) of $LaNbO_4$, $La_{0.995}Sr_{0.005}NbO_4$ and $La_{0.98}A_{0.02}NbO_4$, where A = Ca, Sr or Ba, were synthesized by spray pyrolysis of La–EDTA and Nb–malic acid solutions added dried $A(NO_3)_2$ as described elsewhere [14]. The samples were denoted LN–*y*A where $y = x \times 100\%$ in $La_{1-x}A_xNbO_4$ and LN for pure $LaNbO_4$. As-prepared powders were dry ball milled for 15 min, calcined at 800 °C for 6 h with intermediate stirring, ball milled in 100% ethanol for 24 h, dried in a rotavapor, ground and sieved at 250 μm. Calcined powders were added 4 wt% ethylcellulose as binder.

Pellets (5 and 10 mm Ø) were uniaxially pressed at 100 MPa. Pellets (5 mm Ø) to be exposed to compression had a cylinder length/diameter >2. Bars (~7 mm × 8 mm × 65 mm) were uniaxially pressed at 50 MPa and further cold isostatic pressed at 200 MPa. Green bodies were sintered at 1200 °C for 6 h after binder burn-out at 400 °C. Density was measured by the Archimedes method using isopropanol.

Sintered pellets (10 mm Ø) were polished to 1 μm diamonds for Vickers indentation measurements. The surfaces of the sintered pellets (5 mm Ø) to be exposed to compression were polished to 1 μm diamonds to achieve parallel surfaces, with a deviation in parallelity of <20 μm. The pellets were annealed at 600 °C for 6 h prior to compression. Bars for fracture toughness (K_{IC}) measurements, were machined (Mil. Spec. 1942) to 3 mm × 4 mm × 45 mm with a notch (0.6 mm deep and 0.22 mm wide) by PremaTech Advanced Ceramics, MA, USA. To introduce a V-notch for Single Edge V-Notch Beam (SEVNB) measurements the notches were further cut with a razor blade added 1 μm diamonds to a total maximum depth of 0.63 ± 0.02 mm. The bars were annealed as described for the pellets above.

2.2. Characterization of thermal and mechanical properties

Thermal expansion coefficients (TECs) and transition temperatures (T_c) were determined from linear shrinkage measurements during cooling of cylindrical samples (densification occurred during heating) using a dilatometer (Netzsch DIL 402 E). TECs were determined from the slope of the linear shrinkage as function of temperature. For comparison, the TEC of LN–0.5%Sr was also measured during heating on a 96% dense sample. T_c was determined from the interception between the fitted, extrapolated curves of the linear shrinkage as a function of temperature.

Hardness (H_V) and fracture toughness (K_C) at ambient temperature were calculated using Vickers indentation method (Matsuzawa DVK-1S) on polished surfaces. For hardness measurements, a load of 2.9 N was used and for fracture toughness measurements, a load of 9.8 N (LN–2%Ca and LN–2%Sr) or 98 N (LN–2%Ba) were used for the indentations. For LN–2%Ba a load of 98 N was necessary to create fracture patterns suitable for appropriate calculation of fracture toughness. The surface projected diagonal and crack lengths were measured by optical microscope (Reickert MeF3) or scanning electron microscope (SEM) (Hitachi S-3400N). The fracture toughness was calculated from the average crack length, modulus of elasticity (95 GPa [11]) and measured Vickers hardness using the equation according to Anstis et al. [15].

Fracture toughness and stress–strain relationship during compression were measured in a high temperature testing rig as previously described [16]. Fracture toughness of LN–2%Sr at ambient conditions, and 300 and 600 °C in synthetic air (99.99%) was determined by the single edged V-notched beam (SEVNB) method. A total of 3–6 bars were tested at each temperature, and the fracture toughness was calculated according to ISO 15732 [17]. Further details about the testing are given elsewhere [16]. Stress–strain relationships during compression of LN, LN–0.5%Sr and LN–2%Sr were studied at ambient temperature and atmosphere. LN–0.5%Sr was also studied at 300 and 600 °C in synthetic air (99.99%). Each sample was mounted between two SiC compression plates. A constant load of ~20 N was applied before the load was raised to 2500 N (3500 N for LN–2%Sr). A load/unloading rate of 500 N/min was used. A calibration of the data was performed by measuring the stress–strain relationship of an Al_2O_3 cylinder with known Young's modulus [18], at each temperature. This contribution was subtracted from the strain–stress relationship of each sample. The remnant strain was determined by extrapolating the linear curves to the strain axes.

The domains in LN–0.5%Sr and LN–2%Sr were studied by TEM. The TEM samples were mechanically ground to about 100 μm thickness, dimpled on one side, and finally ion-beam-thinned to electron transparency using a Gatan duo-mill operating at 4.0 kV with a thinning angle of 12°. The discs were cooled by liquid nitrogen during ion milling to reduce ion milling damage of the samples. TEM experiments were performed with a Philips CM30 electron microscope operating at 300 kV.

3. Results

Composition, density, grain size and secondary phases [13] of the different materials are summarized in Table 1. The acceptor doped $LaNbO_4$ had a more homogenous microstructure and smaller grain size compared to pure $LaNbO_4$. TEC and T_c for the different materials are summarized in

Table 1
Relative density, grain size and secondary phases observed for $LaNbO_4$ and $La_{1-x}A_xNbO_4$.

	Density (%)	Grain size (μm)	Secondary phase
$LaNbO_4$	95	13	None
$Ca_{0.02}La_{0.98}NbO_4$	97	1.2	$Ca_2Nb_2O_7$
$Sr_{0.005}La_{0.995}NbO_4$	97	7.0	None/traces[a]
$Sr_{0.02}La_{0.98}NbO_4$	98	2.4	$SrNb_2O_6$
$Ba_{0.02}La_{0.98}NbO_4$	97	2.5	$BaNb_2O_6$

[a] Traces of secondary phases observed after sintering at 1200 °C, but no secondary phase observed after sintering at 1500 °C.

Table 2
Thermal expansion coefficients measured during cooling (TEC) and transition temperatures (T_c) for $LaNbO_4$ and $La_{1-x}A_xNbO_4$.

	TEC monoclinic (10^{-6} °C^{-1})	TEC tetragonal (10^{-6} °C^{-1})	$T_c \pm 10$ (°C)
$LaNbO_4$	14	8.4	504
$Ca_{0.02}La_{0.98}NbO_4$	12	8.3	504
$Sr_{0.005}La_{0.995}NbO_4$	14	8.4	510
$Sr_{0.005}La_{0.995}NbO_4$[a]	18	8.1	501
$Sr_{0.02}La_{0.98}NbO_4$	14	9.1	492
$Ba_{0.02}La_{0.98}NbO_4$	14	8.8	514

[a] Measured during heating of a dense sample.

Table 2. The TEC of the tetragonal high temperature phase ($\sim 8.6 \pm 0.5 \times 10^{-6}$ °C^{-1}) is as expected not influenced by the small variation of the alkaline earths content. The TEC of the monoclinic phase is significantly higher than the one for the tetragonal phase (in the range $12–18 \times 10^{-6}$ °C^{-1}) and is connected with a larger uncertainty. T_c for the different materials is in the range of 492–514 °C. TEC for LN is comparable to the observed values by Takagi et al. [11] and T_c for LN is in agreement with literature [2–5].

The hardness and fracture toughness calculated from Vickers indents are shown in Fig. 1. An increase in hardness from ~3 to ~6 GPa was observed for LN–2%A compared to LN. There was no significant difference in hardness and fracture toughness among the LN–2%A materials. Cracks also appeared from the corners of the indents even at a load of 2.9 N as can be seen from the optical microscope image of LN–2%Sr in Fig. 2. LN–2%Ca showed similar indents. Mainly intergranular cracks were observed after indentation in LN–2%A. SEM image of LN with an indent of 49 N is also included in Fig. 2. Cracks propagate from both the corners and the edges through the grain boundaries, thus, it was not possible to determine the fracture toughness of LN from these indents.

The stress–strain relationships of LN, LN–0.5%Sr and LN–2%Sr are shown in Fig. 3. The remnant strain decreased with increasing Sr-content, from 0.13% for LN to 0.03% for LN–2%Sr. Heat treatment of LN–0.5%Sr to 1500 °C (dotted line in Fig. 3) increased the remnant strain from 0.08% to 0.13%.

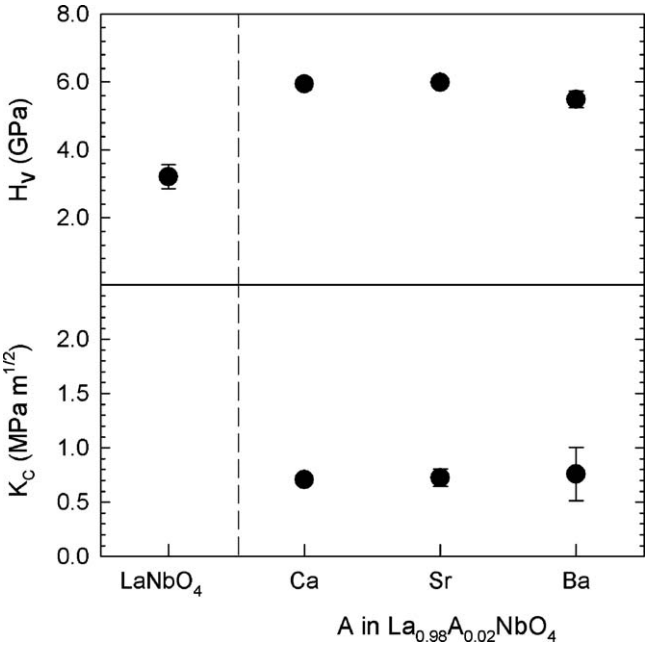

Fig. 1. Hardness and fracture toughness determined from Vickers indentations for $LaNbO_4$, $La_{0.98}Ca_{0.02}NbO_4$, $La_{0.98}Sr_{0.02}NbO_4$ and $La_{0.98}Ba_{0.02}NbO_4$. Error bars show standard deviation.

A maximum stress of ~220 MPa was applied to LN and LN–0.5%Sr as these materials fractured at about 320 MPa. The remnant strain of LN–0.5%Sr sintered at 1200 °C decreased from 0.08% to 0.03% by increasing temperature up to 600 °C (Fig. 4).

The ferroelastic domains in LN–0.5%Sr and LN–2%Sr sintered at 1200 °C are illustrated in Fig. 5. All the images are viewed down along the monoclinic [0 1 0] zone axis, as shown on the two inset diffraction patterns. The split of the diffraction spots is due to the two ferroelastic domains, which alternate across the grains in the bright field images. The width of the domains in LN–0.5%Sr was 10–50 nm while in LN–2%Sr the width was 10–20 nm.

Fracture toughness of LN–2%Sr measured by the SEVNB method as a function of temperature is shown in Fig. 6. The fracture toughness is 1.7 ± 0.2 MPa m$^{1/2}$ independent of

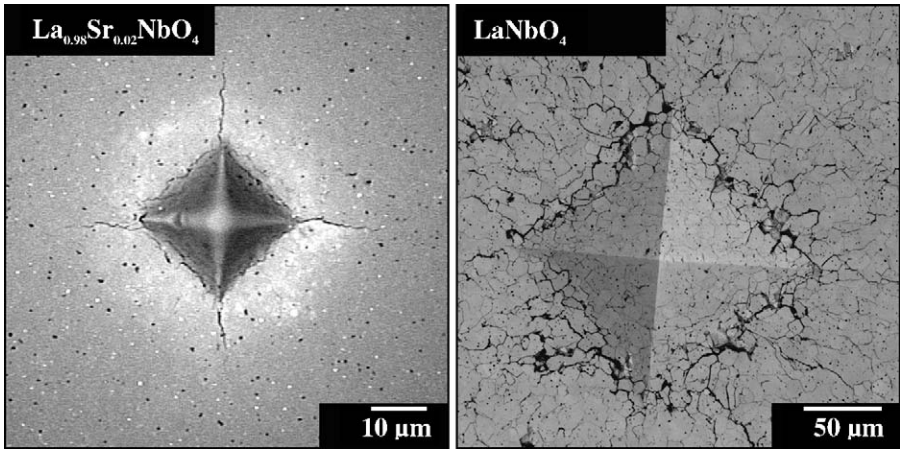

Fig. 2. Optical microscope image of $La_{0.98}Sr_{0.02}NbO_4$ with an indent of 2.9 N and SEM micrograph of $LaNbO_4$ with an indent of 49 N.

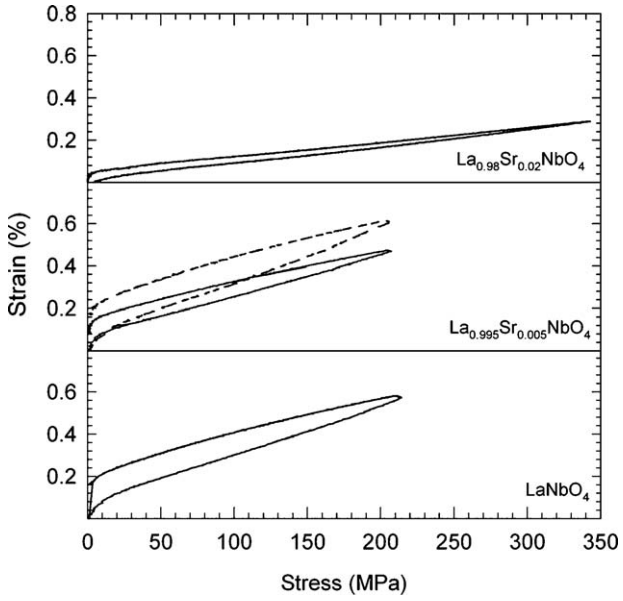

Fig. 3. Stress–strain relationship for $LaNbO_4$, $La_{0.995}Sr_{0.005}NbO_4$ and $La_{0.98}Sr_{0.02}NbO_4$ measured at ambient conditions. All samples were sintered at 1200 °C for 6 h, but one $La_{0.995}Sr_{0.005}NbO_4$ sample (dotted curve) was reheated to 1500 °C for 6 h after sintering.

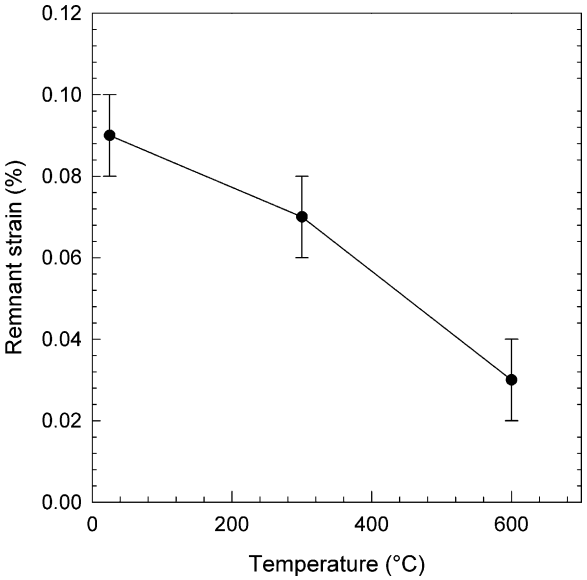

Fig. 4. Remnant strain of $La_{0.995}Sr_{0.005}NbO_4$ as function of temperature in synthetic air.

temperatures up to 600 °C. Fracture surfaces of LN–2%Sr after the SEVNB measurement are shown in Fig. 7. At ambient temperature and 300 °C mainly intergranular cracks were observed, while at 600 °C mainly transgranular cracks appeared.

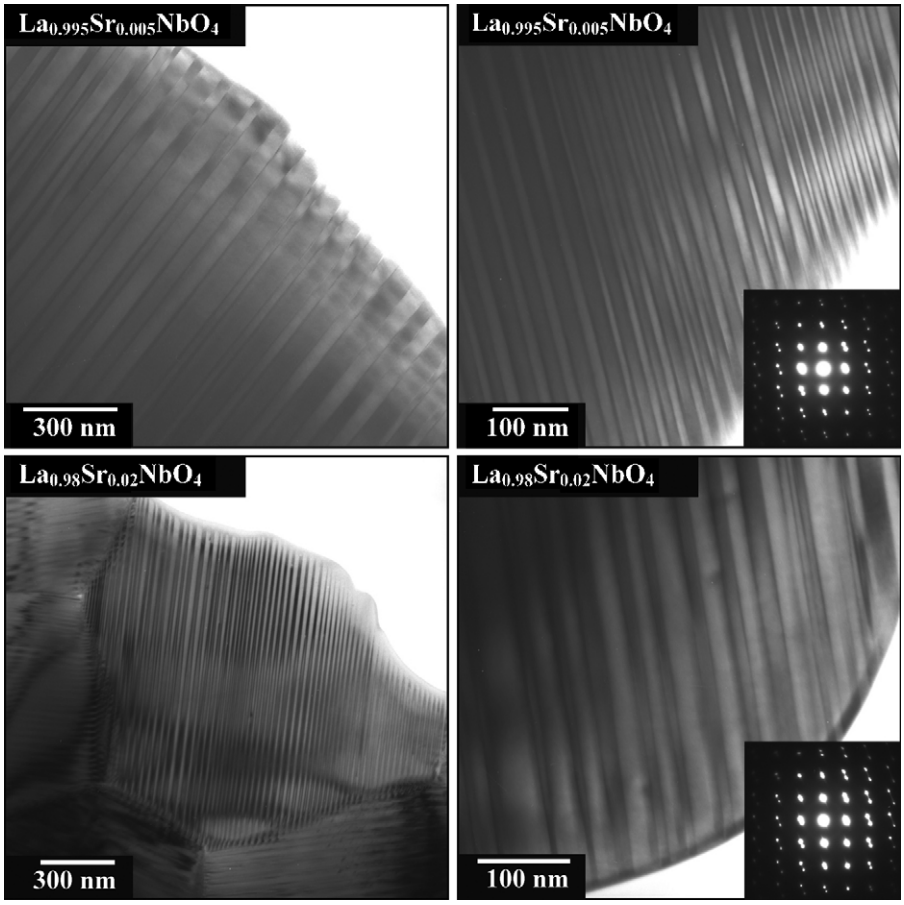

Fig. 5. TEM micrographs of $La_{0.995}Sr_{0.005}NbO_4$ and $La_{0.98}Sr_{0.02}NbO_4$ presenting ferroelastic twins in the materials. Insets show electron diffraction pattern viewed down along [0 1 0] zone axis.

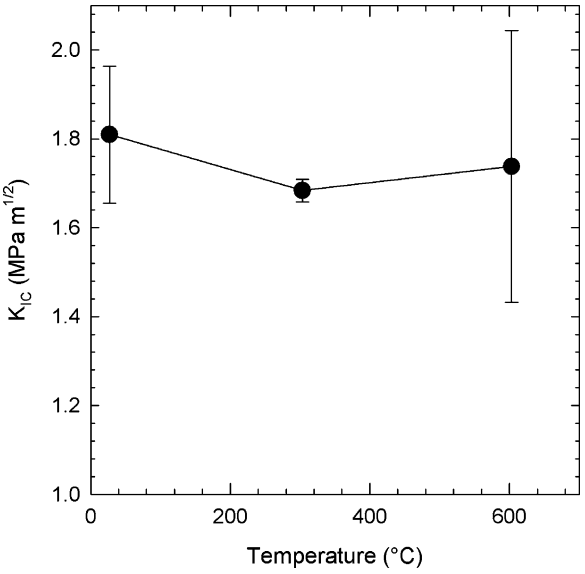

Fig. 6. Fracture toughness of $La_{0.98}Sr_{0.02}NbO_4$ measured by SEVNB as function of temperature in synthetic air. Error bars show standard deviation.

4. Discussion

As shown in Fig. 1, the LN–2%A materials have a significantly higher hardness compared to LN. The fracture pattern in LN (Fig. 2) after indentation shows intergranular cracks both at corners and edges. Since LN has a larger grain size compared to the other materials (Table 1), microcracking due to crystallographic anisotropy is more likely to occur in this material. The lower hardness of LN compared to the acceptor doped materials can therefore be attributed to larger grain size, microcracking or higher porosity. The difference in mechanical properties between pure LN and LN–2%Sr is also evident by the large difference in stress-strain relationship, where LN–2%Sr appears much stiffer than LN.

The stress–strain relationship observed at ambient temperature (Fig. 3) is non-elastic due to ferroelastic domain reorientation. The remnant strain after deloading decreased with Sr content, LN > LN–0.5%Sr > LN–2%Sr. The remnant strain of LN, 0.13%, is in agreement with the work of Jian and Wayman [12], who reported a value of 0.17% calculated by length change and a maximum strain of 5% during exposure to a stress of 200 MPa. The maximum strain reported by Jian and Wayman [12] is however almost tenfold the value reported here. Traces of secondary phase were observed in the acceptor doped samples sintered at 1200 °C. Heat treatment of LN–0.5%Sr to 1500 °C, where the solubility of secondary phases should be larger, increased the remnant strain. Thus, we propose that the presence of secondary phase [18], could inhibit the domain reorientation or pin the domain boundaries. As depicted in Fig. 5, the domain width is smaller in LN–2%Sr compared to LN–0.5%Sr which might be linked to increased amount of secondary phase in LN–2%Sr, decreasing the size of the ferroelastic domains. The narrower stress–strain hysteresis for $La_{0.98}Sr_{0.02}NbO_4$ might also be related to the smaller grain size of this material.

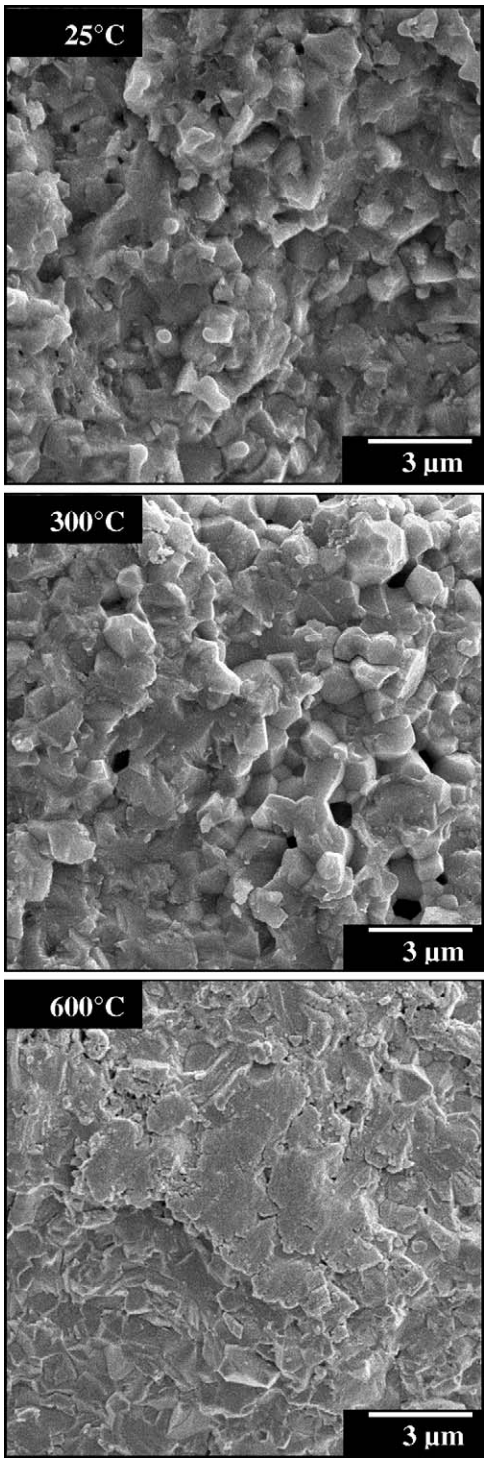

Fig. 7. Micrographs of fracture surfaces of $La_{0.98}Sr_{0.02}NbO_4$ after SEVNB measurements at ambient conditions, and 300 and 600 °C in synthetic air.

The domain width observed here is smaller compared to the domain thickness of 20–300 nm observed in $La_{0.95}Sr_{0.05}NbO_4$ by Prytz and Taftø [19], however their material was also prepared in a different manner. The domain boundary orientation $(2\,0\,-k)/(k\,0\,2)$ in LN–0.5%Sr and LN–2%Sr can be predicted by a simple geometrical model using either electron diffraction patterns or calculated from lattice para-

Table 3
Domain boundary orientation in $La_{0.995}Sr_{0.005}NbO_4$ and $La_{0.98}Sr_{0.02}NbO_4$ predicted from electron diffraction patterns and calculated from lattice parameters according to Eq. (1).

	$La_{0.995}Sr_{0.005}NbO_4$	$La_{0.98}Sr_{0.02}NbO_4$
Electron diffraction pattern	(2 0 −5.08)/(5.08 0 2)	(2 0 −4.96)/(4.96 0 2)
Lattice parameters	(2 0 −5.02)/(5.02 0 2)	(2 0 −5.01)/(5.01 0 2)

meters [14] using Eq. (1):

$$k = \frac{-4ac\cos\beta \pm 2\sqrt{4a^2c^2\cos^2\beta - 2a^2c^2 + a^4 + c^4}}{a^2 - c^2} \quad (1)$$

where a and c are the lattice parameters and β is the angle between a and c in the monoclinic phase [19]. The TEM observations for LN–0.5%Sr and LN–2%Sr are summarized in Table 3. No significant difference in domain boundary orientation is observed between the different samples and preparation methods, which are in agreement with previous data [19,20].

The remnant strain of LN–0.5%Sr decreased with increasing temperature as shown in Fig. 4. This decrease is expected, as the monoclinic distortion decreases, and hence the non-zero strain tensor components decrease, when approaching the phase transition temperature [21]. Furthermore, the domain size is expected to increase close to the phase transition temperature [21]. Above the phase transition temperature, where the material is reported to be paraelastic [22] and no remnant strain is expected, still a low value of 0.03% was measured.

The fracture toughness of LN–2%Sr measured by the SEVNB method (Fig. 6) shows no dependence of temperature up to 600 °C. A ferroelastic material should in principle have enhanced fracture toughness decreasing with increasing temperature, however as the remnant strain in LN–2%Sr is low, no significant effect on the fracture toughness is expected for this material.

Usually, the fracture mode is dependent on grain size, and intergranular fractures are most common in materials with small grains [23]. Therefore, intergranular fracture mode is expected in LN–2%Sr (grain size ∼2 μm). This was observed below the transition temperature (Fig. 7). The change to transgranular fracture mode at 600 °C might to be related to the phase transition from monoclinic to tetragonal. The change into higher symmetry should cause less stress at the grain boundaries, due to a combination of lower anisotropy and lower thermal expansion coefficient, with the result that transgranular crack propagation is favorable. This may explain why the fracture toughness was not dependent on the ferroelastic to paraelastic phase transition.

5. Conclusion

$La_{1-x}A_xNbO_4$ ($x = 0$, 0.005, 0.02 and A = Ca, Sr and Ba) materials possess a ferroelastic to paraelastic phase transition at ∼500 °C with thermal expansion coefficients of $15 \pm 3 \times 10^{-6}$ and $\sim 8.6 \pm 0.5 \times 10^{-6}\,°C^{-1}$ below and above the phase transition temperature. Pure $LaNbO_4$ had lower Vickers hardness (∼3 GPa) compared to $La_{0.98}A_{0.02}NbO_4$ (A = Ca, Sr and Ba) (∼6 GPa) due to significantly larger grain size and possibly microcracking due to crystalline anisotropy. The stress–strain relationship during compression demonstrated the ferroelastic behavior of the $LaNbO_4$-based materials. Small domains (10–50 nm) dependent on composition were observed in $La_{0.995}Sr_{0.005}NbO_4$ and $La_{0.98}Sr_{0.02}NbO_4$. The fracture toughness of $La_{0.98}Sr_{0.02}NbO_4$, measured by SEVNB, was 1.7 ± 0.2 MPa $m^{1/2}$ independent of temperature up to 600 °C. The fracture toughness, measured by the indentation method, was similar (∼0.7 MPa $m^{1/2}$) for all the acceptor doped $LaNbO_4$ materials. A change from intergranular fracture ($T < T_c$) to a transgranular fracture ($T > T_c$) was observed for $La_{0.98}Sr_{0.02}NbO_4$.

Acknowledgement

Work was supported by the Research Council of Norway, Grant No. 1585171431 (NANOMAT).

References

[1] R. Haugsrud, T. Norby, Proton conduction in rare-earth ortho-niobates and ortho-tantalates, Nat. Mater. 5 (3) (2006) 193–196.
[2] L. Jian, C.M. Wayman, Monoclinic-to-tetragonal phase transformation in a ceramic rare-earth orthoniobate, $LaNbO_4$, J. Am. Ceram. Soc. 80 (3) (1997) 803–806.
[3] V.S. Stubican, High-temperature transitions in rare-earth niobates and tantalates, J. Am. Ceram. Soc. 47 (2) (1964) 55–58.
[4] H. Takei, S. Tsunekawa, Growth and properties of $LaNbO_4$ and $NdNbO_4$ single-crystals, J. Cryst. Growth 38 (1) (1977) 55–60.
[5] L.H. Brixner, J.F. Whitney, F.C. Zumsteg, G.A. Jones, Ferroelasticity in $LnNbO_4$-type rare-earth niobates, Mater. Res. Bull. 12 (1) (1977) 17–24.
[6] S. Tsunekawa, H. Takei, Domain switching behavior of ferroelastic $LaNbO_4$ and $NdNbO_4$, J. Phys. Soc. Jpn. 40 (5) (1976) 1523–1524.
[7] K.D. Kreuer, On the development of proton conducting materials for technological applications, Solid State Ionics 97 (1–4) (1997) 1–15.
[8] N. Bonanos, B. Ellis, K.S. Knight, M.N. Mahmood, Ionic-conductivity of gadolinium-doped barium cerate perovskites, Solid State Ionics 35 (1–2) (1989) 179–188.
[9] H. Iwahara, H. Uchida, K. Ono, K. Ogaki, Proton conduction in sintered oxides based on $BaCeO_3$, J. Electrochem. Soc. 135 (2) (1988) 529–533.
[10] H. Iwahara, T. Esaka, H. Uchida, N. Maeda, Proton conduction in sintered oxides and its application to steam electrolysis for hydrogen-production, Solid State Ionics 3–4 (1981) 359–363.
[11] T. Takagi, Y.-H. Choa, T. Sekino, K. Niihara, Fabrication and mechanical properties of $LaNbO_4$ and $LaNbO_4/Al_2O_3$, Key Eng. Mater. 161–163 (1999) 181–184.
[12] L. Jian, C.M. Wayman, Compressive behavior and domain-related shape memory effect in $LaNbO_4$ ceramics, Mater. Lett. 26 (1–2) (1996) 1–7.
[13] T. Mokkelbost, I. Kaus, R. Haugsrud, T. Norby, T. Grande, M.-A. Einarsrud, High temperature proton conducting $LaNbO_4$-based materials. Part II. Sintering properties and solubility of alkaline earth oxides, J. Am. Ceram. Soc. 91 (3) (2008) 879–886.
[14] T. Mokkelbost, Ø. Andersen, R.A. Strøm, K. Wiik, T. Grande, M.-A. Einarsrud, High temperature proton conducting $LaNbO_4$-based materials. Powder synthesis by spray pyrolysis, J. Am. Ceram. Soc. 90 (11) (2007) 3395–3400.
[15] G.R. Anstis, P. Chantikul, B.R. Lawn, D.B. Marshall, A critical evaluation of indentation techniques for measuring fracture toughness. 1. Direct crack measurements, J. Am. Ceram. Soc. 64 (9) (1981) 533–538.
[16] H.L. Lein, Ø.S. Andersen, P.E. Vullum, E. Lara-Curzio, R. Holmestad, M.-A. Einarsrud, T. Grande, Mechanical properties of mixed conducting

$La_{0.5}Sr_{0.5}Fe_{1-x}Co_xO_3$ materials, J. Solid State Electrochem. 10 (2006) 635–642.
[17] ISO/CD 15732, International Organization for Standardization, Geneva, Switzerland.
[18] D.W. Richerson, Modern Ceramic Engineering: Properties, Processing and Use in Design, Marcel Dekker, Inc., NY, USA, 1992.
[19] Ø. Prytz, J. Taftø, Accurate determination of domain boundary orientation in $LaNbO_4$, Acta Mater. 53 (2) (2005) 297–302.
[20] S. Tsunekawa, H. Takei, Twinning structure of ferroelastic $LaNbO_4$ and $NdNbO_4$ crystals, Phys. Status Solidi A 50 (2) (1978) 695–702.
[21] E.K.H. Salje, Phase Transitions in Ferroelastic and Co-elastic Crystals, University Press, Cambridge, UK, 1990.
[22] W.I.F. David, The high-temperature paraelastic structure of $LaNbO_4$, Mater. Res. Bull. 18 (6) (1983) 749–756.
[23] R.W. Rice, Mechanical Properties of Ceramics and Composites: Grain and Particle Effects, Marcel Dekker, Inc., New York, 2005.